

# A Wireless Micro Inertial Measurement Unit (IMU)

Fabian Höflinger, Jörg Müller, Rui Zhang, Leonhard M. Reindl, *Member, IEEE*, and Wolfram Burgard

**Abstract**—In this paper, we present a wireless micro inertial measurement unit (IMU) with the smallest volume and weight requirements available at the moment. With a size of  $22\text{ mm} \times 14\text{ mm} \times 4\text{ mm}$  ( $1.2\text{ cm}^3$ ), this IMU provides full control over the data of a three-axis accelerometer, a three-axis gyroscope, and a three-axis magnetometer. It meets the design prerequisites of a space-saving design and eliminates the need for hard-wired data communication, while still being competitive with state-of-the-art commercially available MEMS IMUs. A CC430 microcontroller sends the collected raw data to a base station wirelessly with a maximum sensor sample rate of 640 samples/s. Thereby, the IMU performance is optimized by moving data post processing to the base station. This development offers important features in portable applications with their significant size and weight requirements. Due to its small size, the IMU can be integrated into clothes or shoes for accurate position estimation in mobile applications and location-based services. We demonstrate the performance of the wireless micro IMU in a localization experiment where it is placed on a shoe for pedestrian tracking. With sensor data-fusion based on a Kalman filter combined with the zero velocity update, we can precisely track a person in an indoor area.

**Index Terms**—Indoor localization system, inertial measurement unit (IMU), wireless sensor.

## I. INTRODUCTION

IN RECENT years, location-based services for indoor mobile devices are becoming more and more popular due to their increasing functional range. To effectively direct people in their environments, for example, to specific products or to particular exhibition booths, an accurate localization system is needed. In indoor applications, where typically no GPS signal is available, one promising localization approach, e.g., for cell phones or mobile robots, relies on inertial sensors.

In the domain of mobile robots, inertial sensors are commonly used to improve odometry [1] or for flight stabilization or autonomous hovering of helicopters or quadrotors [2]. Furthermore, inertial sensors have been applied for localization of airplanes and miniature indoor blimps [3], [4].

For human tracking, miniature inertial sensors can be integrated into clothes or shoes [5]–[8]. The inertial measurement units (IMUs) can extend the functionality of pedometers by

full 3-D location information. Even more complex tasks such as full-body human motion capture have been addressed using inertial sensors [9]. Additionally, the combination of inertial sensors with wireless signal sensors [10] allows for correction of the errors accumulated during integration of inertial sensor data as shown by Xsens with the MVN MotionGrid. Similarly, personal devices such as cell phones can be localized inside of buildings.

However, due to their size, weight or power consumption, commercially available IMUs are not ideally suited for certain applications, such as miniature aerial vehicles [4], [11], [12] or inconspicuous integration into clothes or shoes.

## II. STATE-OF-THE-ART INERTIAL MEASUREMENT UNITS (IMU)

Today, many different IMUs are available commercially. Fig. 1 shows an overview of the dimensions and the performance data of commercial state-of-the-art IMUs and those developed by scientific research groups. The performance of an IMU is typically characterized by the bandwidth, drift, linearity and sample rate of its sensors. For portable applications, IMUs with small dimensions are essential. In contrast to the commercial products, existing research prototypes are typically smaller and lighter. However, for precise data processing and state estimation in dynamic applications high raw data rates are required, which is a bottleneck in the development of IMU designs.

For the stability of the sensor output a minimum sensor drift is necessary. Especially, the drift of the gyroscope is crucial since it cannot be reset during the measurement phase. IMUs with a low sensor drift and a high sensor performance typically have large dimensions and communicate to computers by cable. High-performance devices, such as the NG LITEF IMUs for civil and military aviation, are equipped with hermetically sealed cases and fiberoptic gyroscopes that provide low noise, high stability, and a low drift factor. In contrast to that, the NG LITEF  $\mu$ IMU-I [13] is based on microelectromechanical systems (MEMS) gyroscopes and has a size of  $160\text{ cm}^3$ . However, due to their size, weight or power consumption, these IMUs are not suited for mobile applications in small unmanned aerial vehicles and clothes or shoes.

Besides the high-performance devices mentioned above, smaller IMUs, such as the Xsens MTi [14], the Sparkfun Electronics Razor IMU [15], and the X-IMU [16], are commercially available. However, the smaller size comes at the cost of a reduced sensor data performance and compensation accuracy. Whereas the Xsens MTi provides orientation estimates from onboard sensor data fusion and compensated raw sensor

Manuscript received July 9, 2012; revised November 6, 2012; accepted November 8, 2012. Date of publication June 20, 2013; date of current version August 7, 2013. This work was supported by the German Research Foundation within the Research Training Group 1103 (Embedded Microsystems). The Associate Editor coordinating the review process was Dr. Antonios Tsourdos. The authors are with the Albert-Ludwigs University of Freiburg, Freiburg 79110, Germany (e-mail: fabian.hoefflinger@imtek.de; muellerj@informatik.uni-freiburg.de; rui.zhang@imtek.de; reindl@imtek.de; burgard@informatik.uni-freiburg.de).

Color versions of one or more of the figures in this paper are available online at <http://ieeexplore.ieee.org>.

Digital Object Identifier 10.1109/TIM.2013.2255977

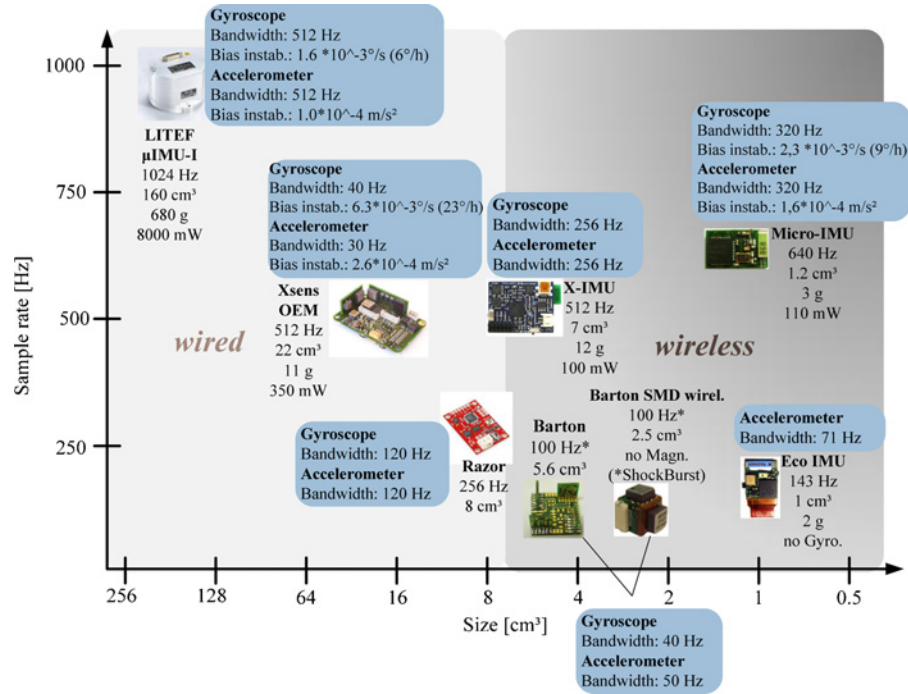


Fig. 1. Overview of the size and the data performances of state-of-the-art IMUs.

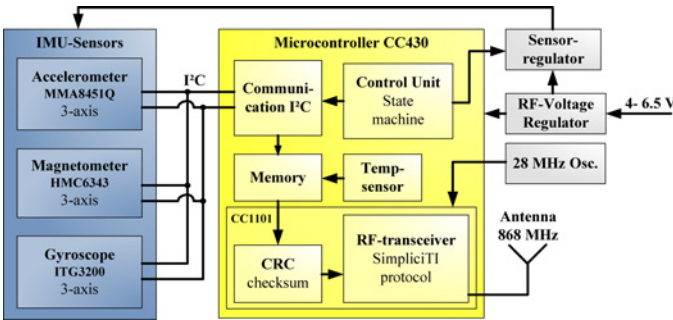


Fig. 2. Block diagram of the micro-IMU.

data, most small-sized IMUs provide only uncompensated raw sensor data. Therefore, the Xsens MTi is the most common small-sized inertial sensor in research.

Apart from commercial products, several research groups have put effort into further enhancement with respect to special characteristics. One important aim, for example, is the miniaturization of the device. Barton *et al.* [17] demonstrated a cubic IMU design and wireless communication. Another approach is the combination of typical accelerometers and gyroscopes with a linear encoder for which Lim *et al.* [18] claim a size of 10 mm × 15 mm. Tsai *et al.* [19] presented a small wireless IMU without gyroscopes in a size of 1 cm<sup>3</sup>. In contrast to these miniature devices, our micro-IMU provides a considerably higher sensor performance and full control over gyroscopes, accelerometers, and magnetometers, while being one of the smallest IMU designs available.

### III. DESIGN OF THE MICRO-IMU

In this paper, we present a wireless micro-IMU [20] that meets the size, format, and power consumption constraints for embedded mobile applications such as the integration into

TABLE I  
SPECIFICATION OF THE SENSORS IMPLEMENTED ON THE MICRO-IMU

Sensor Type	Full-Scale range	Sensitivity	Maximum sampling rate	Digital resolution
Accelerometer MMA8451Q	±4 g	0.003 g	800 samples/s	14 b
Gyroscope ITG3200	2000°/s	0.061°/s	8k samples/s	16 b
Magnetometer HMC6343	±1 Gs	0.1°	10 samples/s	12 b

clothes and shoes. By using MEMS sensors with large scale integration, the performance is still comparable to state-of-the-art commercially available MEMS IMUs. In our micro-IMU we apply modern accelerometers and gyroscopes that feature three-axis technology and integrated analog-to-digital conversion with automatic temperature compensation in a one-chip design. This saves space in the IMU design as analog converters, high precision voltage references and 3-D packaging are not needed. Thus, a four-layer PCB is sufficient for integration of all sensors and a microcontroller.

One important aspect of the design is the decision to move data processing from the IMU to a base station. Through this step, the required processing power and therefore the power consumption of the IMU can be reduced, as the demanding computation of sensor data fusion filters and other algorithms to enhance the data quality is moved to more powerful computers with less constraints in size and weight. In this case, the energy source of the IMU can be minimized in weight and size or the operation time can be increased, respectively. This is important especially for battery-powered embedded microsystems.

The components and the data flow of our micro-IMU are shown in Fig. 2. The CC430 microcontroller is interfaced to

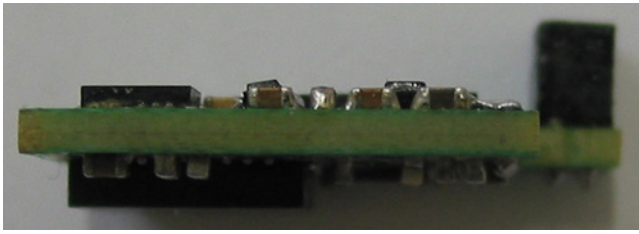


Fig. 3. Micro-IMU V1 side view. The connector at the right top of the IMU can be removed after programming the device.

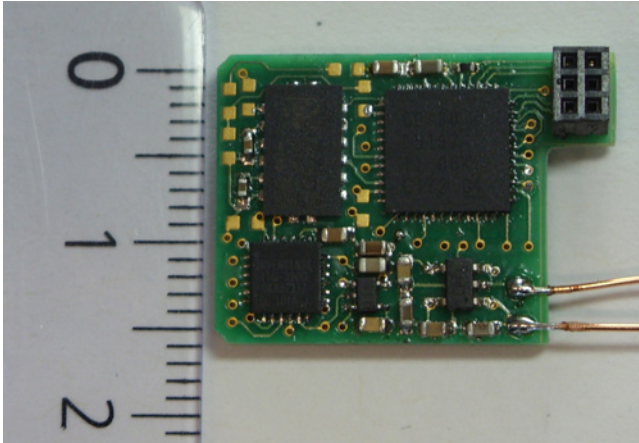


Fig. 4. Micro-IMU V1 top view.

the three-axis accelerometer (MMA8451Q), three-axis magnetometer (HMC6343), and three-axis gyroscope (ITG3200) via the I<sup>2</sup>C protocol. A 28-MHz oscillator is used for the transceiver functionality along with a voltage regulator for the RF-circuitry. Furthermore, a separated voltage regulator for the digital circuitry is used to avoid high frequency distortions in the sensor data.

The sensors are systematically selected for a high data rate and digital resolution while providing the full scale range at the same time.

- 1) *Accelerometer*: The Freescale Semiconductor MMA8451Q low-power three-axis accelerometer with a resolution of 14 b is used. The chip offers a *g*-selection, which allows a selectable full scale of  $\pm 2g$ ,  $\pm 4g$ , or  $\pm 8g$ . According to that, the sensitivity is  $122 \mu g$ ,  $244 \mu g$ , or  $488 \mu g$ , respectively. Additionally, the sensor can be configured to generate inertial wake-up interrupts and provides several low-pass filters, the user can select for a reduction of aliasing effects and noise.
- 2) *Gyroscope*: The digital gyroscope InvenSense ITG3200 is used for measuring the angular rate. The three-axis MEMS gyroscope provides a 16-b resolution and several internal low-pass filters. The sensor offers a full scale of  $2000^\circ/s$  and a maximum sensitivity of  $0.061^\circ/s$ .
- 3) *Magnetometer*: The digital Honeywell HMC6343 magnetometer is used for measuring the geomagnetic field. It has a three-axis magneto-resistive sensor with 12 b of resolution.

Table I shows the configuration and the respective specification of the sensors implemented on the micro-IMU.

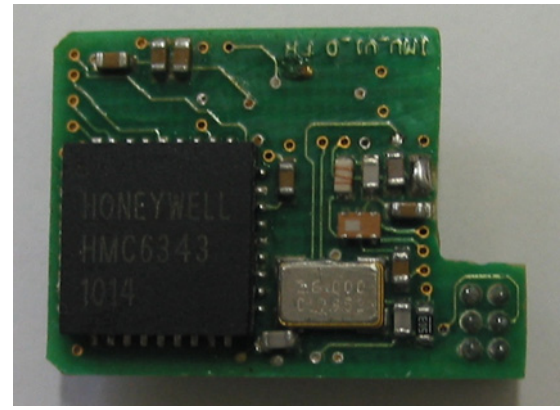


Fig. 5. Micro-IMU V1 bottom view.

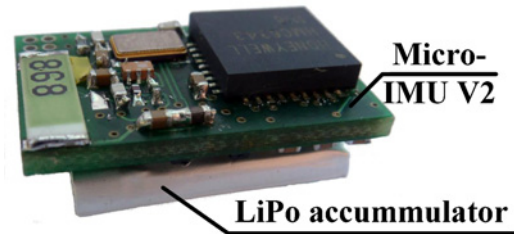


Fig. 6. Micro-IMU V2 with a LiPo accumulator.

For reading the digital sensor data and radio data transmission, we apply a CC430 microcontroller on the micro-IMU. It combines an integrated CC1101 wireless transceiver and an MSP430 microcontroller that is a 16-b RISC mixed-signal processor for ultra-low power applications. The wireless transceiver works in the SRD-Band (a band designed for low-power communication devices), which is specified in the European Union from 863 MHz to 870 MHz with a maximum allowed power output of 10 dBm. The low-power communications protocol SimpliciTI from Texas Instruments is used, as this protocol is efficient due to the minimal frame overhead. The transceiver part of the CC430 supports the maximum allowed power output, i.e., 10 dBm and a maximum radio transmission data rate of 500 kbaud/s. For validation of the communication link, a hardware CRC16 module is implemented on the CC430 so that the full processing power can be used for data acquisition and transmission. In our current configuration the CC430 microcontroller can provide sensor data wirelessly at a maximum sensor sample rate of 640 samples/s with low power consumption.

By choosing QFN-packages and using a four-layer PCB layout, the size of the IMU is reduced almost to the accumulated footprint of the ICs. The two inner layers are floated with ground copper serving as a ground plane for the quarter-wave antenna. The large ground plane acts as the missing half of a dipole antenna and is important for the radiation quality of the antenna. Furthermore, using an increased ground plane reduces the noise floor and minimizes the overall resistance as all devices are connected to this ground plane. The Johanson Technology SWRA250 is used to provide on-chip impedance matching between the transceiver and antenna of the micro-

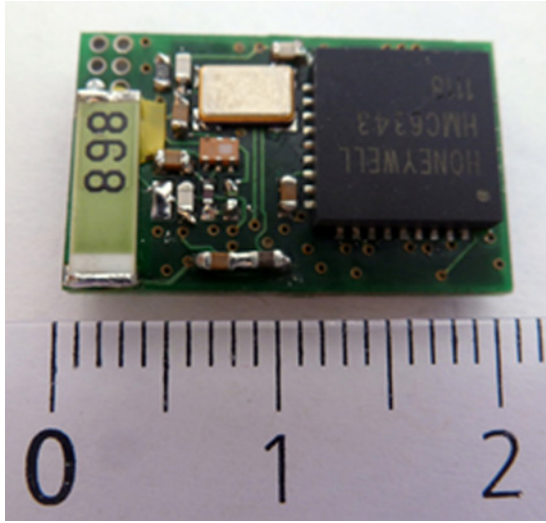


Fig. 7. Top view of the micro-IMU V2 with chip antenna.

IMU. Subsequently, the SWRA250 reduces the size of the matching network that is superior to procedural impedance matching networks.

#### A. Micro-IMU V1

Our first prototype is shown in Figs. 3–5. Instead of a chip antenna, we employ a quarter-wave wire-antenna on the micro-IMU that can be adjusted to the available space on the embedded system. Fig. 3 shows the dimensions of our micro-IMU that are  $18\text{ mm} \times 16\text{ mm} \times 4\text{ mm}$  ( $1.2\text{ cm}^3$ ). The programming port on the top right is optional and can be removed for further size reduction. The high frequency components are implemented in the bottom layer of the PCB (Fig. 5) to avoid high frequency disturbance on the measurements. In the first version of the micro-IMU V1 the acceleration sensor STMicroelectronics LIS3LV02 was used. Because of its non-homogeneous drift and the noise performance with respect to the three axes, we replaced this sensor with the Freescale Semiconductor MMA8451Q.

#### B. Micro-IMU V2

For the implementation of a chip antenna on the micro-IMU, we developed a second prototype. The top view of the redesign is shown in Fig. 7. The size of the IMU is  $22\text{ mm} \times 14\text{ mm} \times 4\text{ mm}$  ( $1.2\text{ cm}^3$ ). Fig. 6 shows the micro-IMU mounted on an accumulator that powers the device for about 1 h of continuous operation.

For reception of the raw IMU sensor data we developed a hardware module that can be connected to a standard PC via USB. For the user's convenience, this hardware module is USB bus-powered, applies a CRC check to the incoming data stream, and automatically deletes invalid packets.

### IV. DATA PROCESSING

One important factor concerning the quality of orientation and positioning estimates is the data post-processing. In the

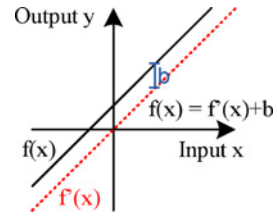


Fig. 8. Offset error of the sensor output.

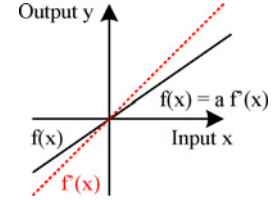


Fig. 9. Scale factor error of the sensor output.

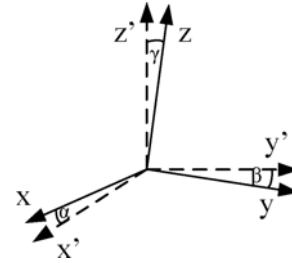


Fig. 10. Angle misalignment of the three axes of the sensor.

following section, we will present techniques for sensor characterization of deviations and error compensation. The error compensation can be implemented as a data post-processing.

#### A. Compensation

Some systematic deviations, namely offset (Fig. 8), temperature drift, scaling factor (Fig. 9), and angle misalignment of each sensor axes (Fig. 10), on the sensor readings can be compensated by calibration. The errors of the sensors are caused by variations in the production process of the sensors and environmental dependencies like the temperature. Each sensor will have its own compensation coefficient, which implies every sensor is required to be characterized [21]. The experimental methods for calibration of the sensors of the micro-IMU are given in Table II. In the following, we briefly describe the individual calibration experiments.

1) *Static and Climate Chamber Experiment:* The offset error

$$O(T) = B + C(T) \quad (1)$$

of the gyroscope and acceleration sensor depends on a static bias error  $B = [b_x \ b_y \ b_z]^T$  and a temperature drift  $C(T) = [f_x(T) \ f_y(T) \ f_z(T)]^T$ . To analyze the offset error of the gyroscope  $O_g(T)$  and the accelerometer  $O_a(T)$ , we statically mount the micro-IMU in a climate chamber and expose it to different temperatures ranging from  $5\text{ }^\circ\text{C}$  to  $55\text{ }^\circ\text{C}$ . For temperature drift and bias compensation, we apply a least-squares cubic spline approximation to the sensor data recorded in the climate chamber, as shown in Figs. 11 and 12.



TABLE II  
METHODS FOR CALIBRATION OF DIFFERENT ERRORS

Errors	Gyroscope	Acceleration Sensor	Magnetic field sensor
Offset error (bias)	Static	Cube	Rotation about all axes
Temperature drift	Climate chamber	Climate chamber	–
Scaling factor (gain)	Rotation table	Cube	Rotation about all axes
Angle misalignment	Rotation table	Cube	Rotation about all axes

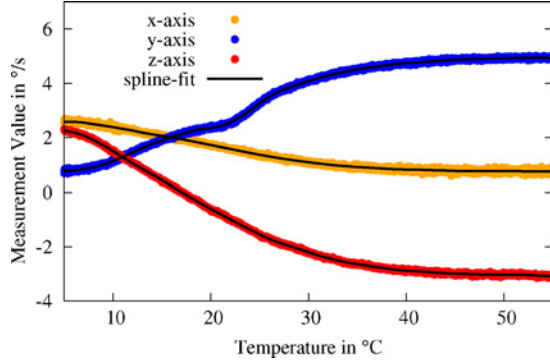


Fig. 11. Temperature drift of the gyroscope ITG3200.

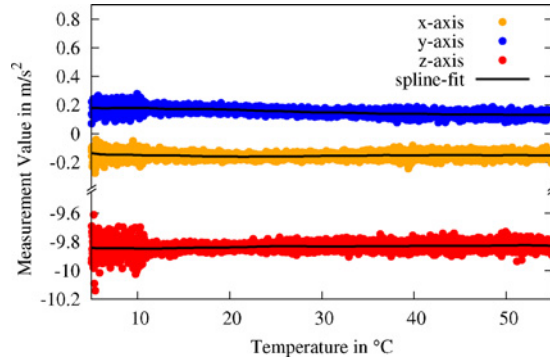


Fig. 12. Temperature drift of the accelerometer MMA8451Q.

Although the implemented digital gyroscope ITG3200 has a built-in temperature compensation, it still exhibits a distinct temperature drift as depicted in Fig. 11. For compensation of the offset error  $O_g(T)$  of the gyroscope, the CC430 microcontroller has an internal temperature diode that can be used to measure the temperature through the internal analog digital converter. The temperature sensor has a linear output over the temperature range from 10 °C to 85 °C. However, its offset error can be large and needs to be calibrated precisely. In our micro-IMU design, we transmit the temperature data wirelessly together with the sensor data to the base station to compensate the offset error of the gyroscope.

The response of the digital accelerometer MMA8451Q, which is shown in Fig. 12, indicates that the noise of the sensor increases with the temperature. This effect is caused by the electronic noise that is generated by the thermal agitation of the charge carriers inside a semiconductor. The increased noise in the first part of the measured sensor response in Fig. 12 is

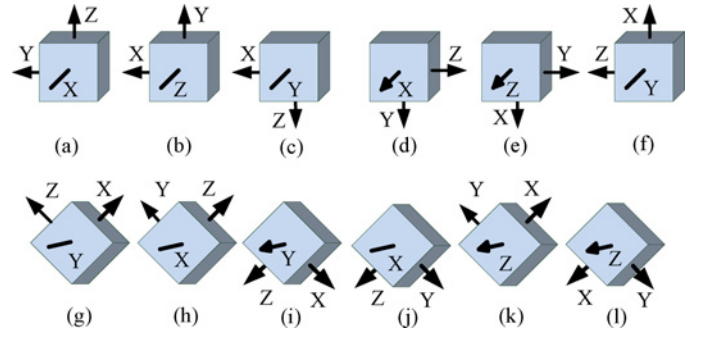


Fig. 13. Twelve positions of the IMU to calibrate the acceleration sensor.

caused by the vibration in the heating mechanics of the climate chamber. Furthermore, Fig. 12 indicates that the accelerometer has no significant temperature drift. Consequently, the offset error of the accelerometer MMA8451Q can be approximated by  $O_a(T) = B_a$ .

2) *Cube Experiment*: The offset error, the scaling factor error, and the angle misalignment of the acceleration sensor are determined in the cube experiment. Taking these errors into account, the measurement  $A = [a_x \ a_y \ a_z]^T$  of the three-axis accelerometer depends on the real acceleration values  $A' = [a'_x \ a'_y \ a'_z]^T$  through

$$A = S_a(A' + B_a) . \quad (2)$$

Here, the matrix

$$S_a = \underbrace{\begin{pmatrix} s_{a,xx} & 0 & 0 \\ 0 & s_{a,yy} & 0 \\ 0 & 0 & s_{a,zz} \end{pmatrix}}_{\text{scaling}} \underbrace{R(\alpha_a, \beta_a, \gamma_a)}_{\text{rotation}} \quad (3)$$

combines the scaling factors and the angle misalignment of the individual measurement axes, given the rotation matrix

$$R(\alpha_a, \beta_a, \gamma_a) = \begin{pmatrix} \cos \beta_a \cos \gamma_a & -\cos \beta_a \sin \gamma_a & \sin \beta_a \\ \cos \alpha_a \cos \gamma_a - \sin \alpha_a \sin \beta_a \sin \gamma_a & \cos \alpha_a \sin \gamma_a + \sin \alpha_a \sin \beta_a \cos \gamma_a & -\sin \alpha_a \cos \beta_a \\ \sin \alpha_a \cos \gamma_a + \cos \alpha_a \sin \beta_a \sin \gamma_a & \sin \alpha_a \sin \gamma_a - \cos \alpha_a \sin \beta_a \cos \gamma_a & \cos \alpha_a \cos \beta_a \end{pmatrix} . \quad (4)$$

Under the assumption that the misalignment angles  $\alpha_a$ ,  $\beta_a$ , and  $\gamma_a$  are very small, the rotation matrix  $R(\alpha_a, \beta_a, \gamma_a)$  can be approximated by the antisymmetric matrix [22]

$$R(\alpha_a, \beta_a, \gamma_a) = \begin{pmatrix} 1 & -\gamma_a & \beta_a \\ \gamma_a & 1 & -\alpha_a \\ -\beta_a & \alpha_a & 1 \end{pmatrix} . \quad (5)$$

To determine the nine unknown parameters  $s_{a,xx}$ ,  $s_{a,yy}$ ,  $s_{a,zz}$ ,  $\alpha_a$ ,  $\beta_a$ ,  $\gamma_a$  and  $b_{a,x}$ ,  $b_{a,y}$ ,  $b_{a,z}$  in (2), we mount the micro-IMU inside of a hollow metal cube, where the sensor axes are aligned with those of the cube. As illustrated in Fig. 13, we place the cube in 12 different positions and measure the accelerations that should match the gravity vector  $g = [0 \ 0 \ 9.81 \text{ m/s}^2]^T$ . Six positions (1, 2, 3, 4, 5, 6) are orthogonal positions to the ground. The other six

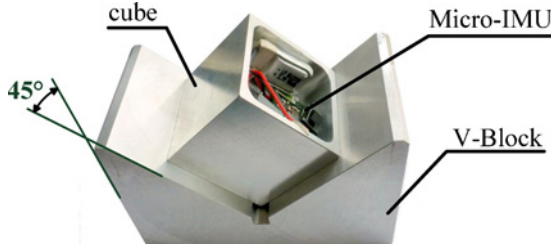


Fig. 14. Setup for the cube experiment.

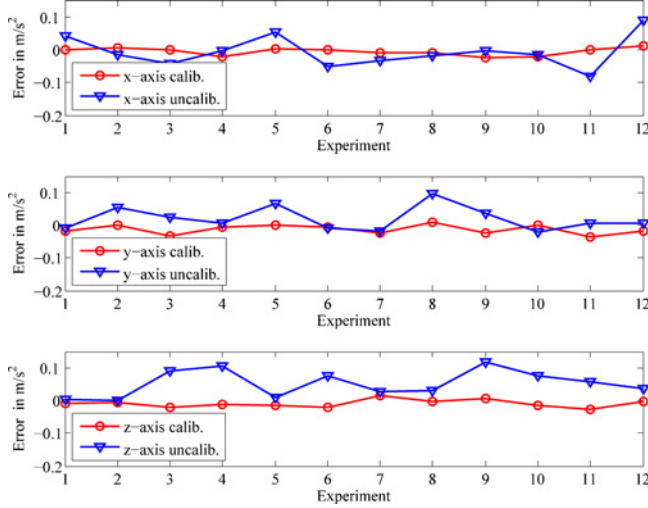


Fig. 15. Errors of the accelerometer output of the three axes in the 12 different positions of the cube experiment and the corresponding errors after calibration.

positions (7, 8, 9, 10, 11, 12) are in  $45^\circ$  to ground using the V-Block depicted in Fig. 14.

We determine the unknown parameters by minimizing the deviation

$$r_a = \sum_{i=1}^{12} \left| \|A'_i\| - \|g\| \right| \quad (6)$$

of the compensated acceleration measurements from the gravity. Fig. 15 shows the errors of the accelerometer output of the three axes in the 12 different positions of the experiment and the corresponding errors after calibration.

3) *Experiment With the Rotation Table:* The scaling factor error and the angle misalignment of the gyroscope is determined in an experiment using the rotation table. Taking these errors into account, the measurement  $\Omega = [\omega_x \ \omega_y \ \omega_z]^T$  of the three-axis gyroscope depends on the real angular speed  $\Omega' = [\omega'_x \ \omega'_y \ \omega'_z]^T$  through

$$\Omega = S_g(\Omega' + O_g(T)) \quad (7)$$

where  $S_g$  includes six unknowns parameters for misalignment and scaling analog to  $S_a$ . As we assume the ambient temperature to be static during the experiment, the temperature drift error can be determined in advance so that the static bias error  $B_g$  is the remaining part of the offset error  $O_g(T)$  to be determined in this experiment.

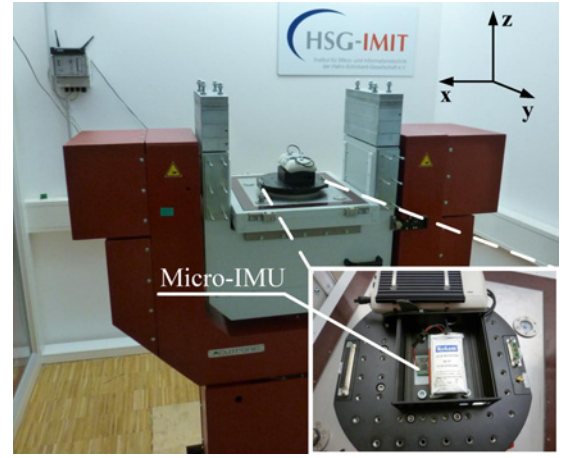


Fig. 16. Rotation table used to calibrate the gyroscope.

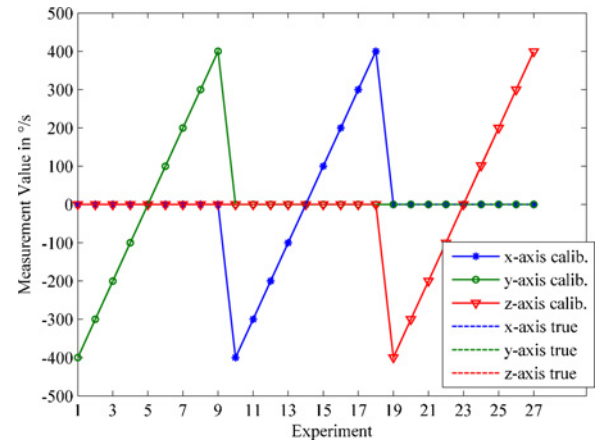


Fig. 17. Output of the uncalibrated gyroscope during the experiment.

We determine the nine unknown parameters by mounting the micro-IMU to a rotation table (Fig. 16), which can rotate the IMU with a constant angular velocity  $\tilde{\omega}$ . In our experiment the micro-IMU was rotated with nine different angular velocities from  $-400^\circ/\text{s}$  till  $400^\circ/\text{s}$  in  $100^\circ/\text{s}$  steps around the  $x$ -, the  $y$ -, and the  $z$ -axis. Analog to the cube experiment, we determine the unknown parameters in an iterative minimization of the deviation

$$r_g = \sum_{i=1}^{27} \left| \|\Omega'_i\| - \tilde{\omega}_i \right| \quad (8)$$

of the compensated angular velocity measurements from the reference values of the angular velocity.

Fig. 17 shows the output of the uncalibrated gyroscope and the true values during the experiment, which illustrates the scaling error of the uncalibrated sensor. Fig. 18 shows the calibrated data of the gyroscope and the reference values of the rotation table.

4) *Rotation About All Axes Experiment:* The offset error, the scaling factor error, and the angle misalignment of the magnetometer are determined in the rotation about all axes experiment. Taking these errors into account, the measurement  $M = [m_x \ m_y \ m_z]^T$  of the three-axis magnetometer depends on

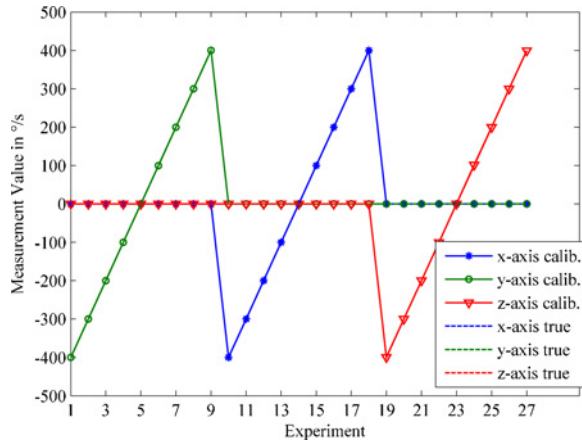


Fig. 18. Output of the calibrated gyroscope.

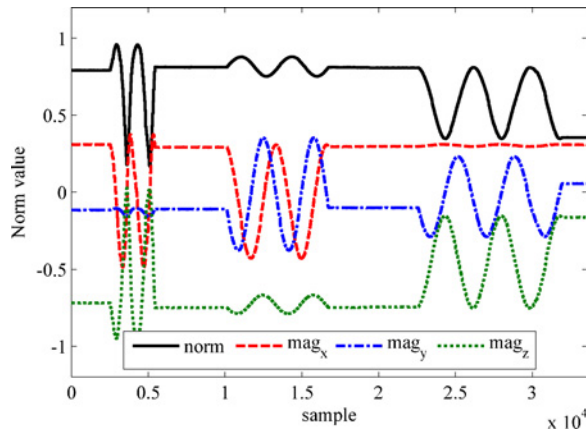


Fig. 19. Raw data of the magnetic field sensor.

the real magnetic field  $M' = [m'_x \ m'_y \ m'_z]^T$  through

$$M = S_m(M' + B_m) \quad (9)$$

where  $S_m$  includes the scale factor and angle misalignment compensation and  $B_m$  the offset compensation.

To determine  $B_m$  and  $S_m$  we mounted the IMU on a robot without any metallic materials and rotated it around all three axes on a green field outdoors to read the magnetometer. In contrast to the passive surroundings on the green field, ferromagnetic materials (steel, nickel, and iron) affect the magnetic field [23]. For the calibration of earth's magnetic field compass, the sensors should have a sufficient distance from ferrous objects that could not bend the fields and cause a systematical error.

In our calibration approach, we choose the scaling of the magnetic field so that the earth's magnetic field has a norm of 1. Based on that, we determine  $B_m$  and  $S_m$  using a linear optimization on

$$r_m = \sum_{i=1}^N M_i'^T M_i' - 1 \quad (10)$$

through singular value decomposition.

Fig. 19 shows the uncalibrated and Fig. 20 the calibrated magnetic field measurements recorded during the calibration

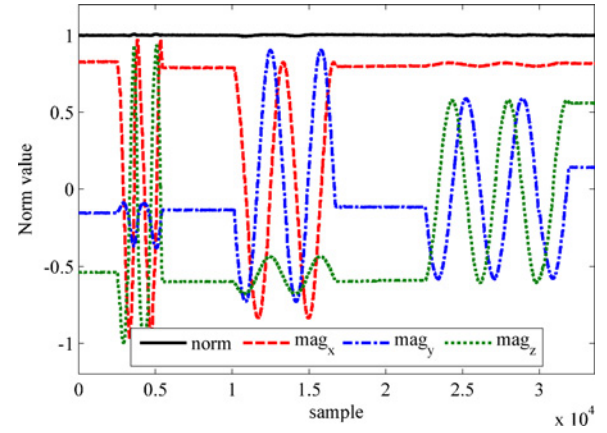


Fig. 20. Output data of the magnetic field sensor after calibration.

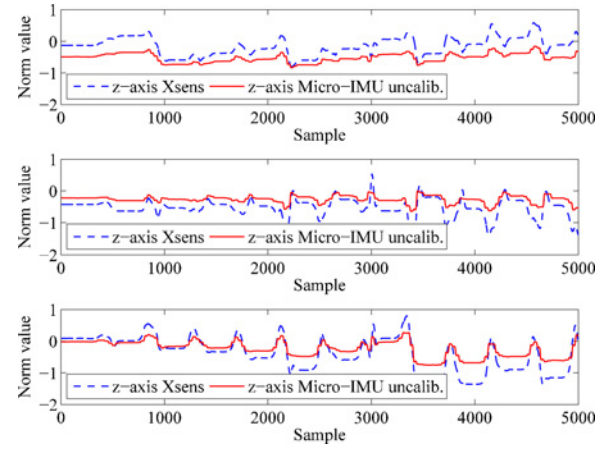


Fig. 21. Output of the uncalibrated magnetometer during a walk.

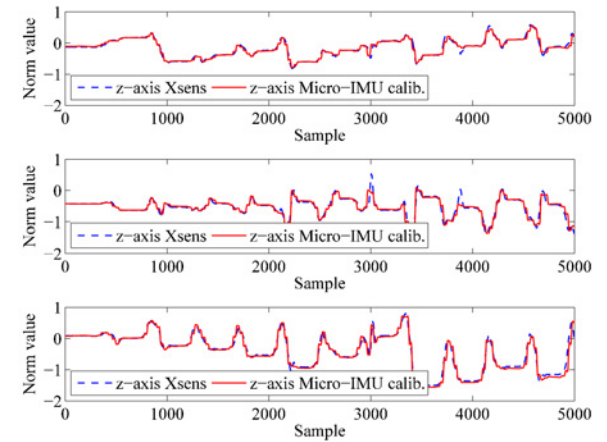


Fig. 22. Output of the calibrated magnetometer during a walk.

experiment. The norm  $\|M'\|$  represents the earth's magnetic field strength. It can be seen that after calibration, the scalar error and bias has been removed and the norm or the calibrated measurements of the earth's magnetic field strength remains close to 1.

Fig. 21 shows the data of the uncalibrated magnetic field measurements of the micro-IMU during a short walk compared to that of the factory calibrated Xsens MTi. After calibration,



TABLE III  
COMPARISON BETWEEN UNCALIBRATED AND CALIBRATED SENSORS

Errors	Gyroscope	Accelerometer	Magnetometer
Uncalibrated	25.64°/s	0.052 m/s <sup>2</sup>	14.69 nT
Calibrated	0.15°/s	0.015 m/s <sup>2</sup>	3.90 nT

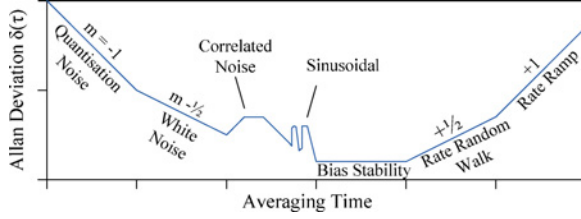


Fig. 23. Schematic diagram of the Allan variance.

Fig. 22 shows that the deviation of the calibrated measurements of the micro-IMU from that of the Xsens MTi is minimized.

#### B. Comparison Between Uncalibrated and Calibrated Measurements

For calculating the errors of the uncalibrated sensor data  $Z$  and the calibrated sensor data  $Z'$ , the root mean square

$$Z_{RMS} = \sqrt{\frac{1}{N} \sum_{n=1}^N (Z - Z')^2} \quad (11)$$

of the deviations in the individual experiments are calculated. The errors of the uncalibrated and the calibrated measurements of the accelerometer, the gyroscope and the magnetometer are shown in Table III.

#### C. Evaluation of Measurement Error and Allan Variance

After compensation of static measurement deviations, the measurement data quality is determined through the evaluation of the bias-drift and the measurement noise. The drift of the measurement values of the gyroscopes and accelerometers has a devastating effect on the on accuracy of an IMU as it leads to a quadratic effect on the position estimated by integration of the measurement data.

To gain knowledge about the magnitude of drift and noise, we evaluate the Allan variance  $\sigma_a^2$  of the measurement data. The Allan variance is an instrument for representing the root mean square random drift errors as a function of averaging time intervals  $\Delta t$  [24]. It is defined as

$$\sigma_a^2(\Delta t) = \frac{1}{2(N-1)} \sum_{i=1}^{N-1} (x_i - x_{i-1})^2 \quad (12)$$

depending on the differences between consecutive measurements of the sensor data recorded at the measurement period  $\Delta t$ .

The graph of the Allan variance expresses five types of noise terms with various gradients, as shown in Fig. 23: random walk, rate random, bias instability, quantization noise, and rate ramp. White noise or random walk appears with a gradient of  $-0.5$  on the diagram of the Allan variance. The noise based

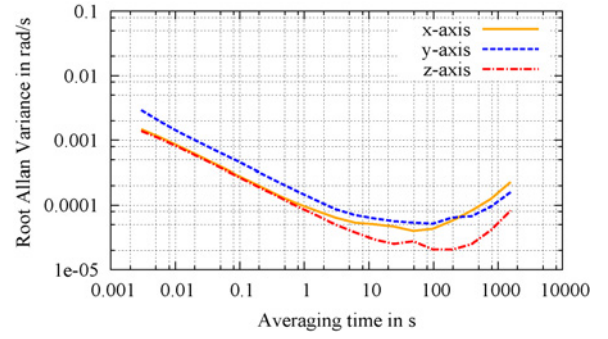


Fig. 24. Allan variance of the gyroscope ITG3200 of the micro-IMU.

on a bandwidth of 1 Hz is identified by fitting a straight line through the slope of the curve at the averaging time of 1 s. The bias instability is defined as the flat region around the minimum of the graph. The drift value can be identified as the global minimum of the Allan variance.

#### D. Evaluation Results

For the sensor characterization by means of the Allan variance, we first captured the raw sensor data of the micro-IMU V2 for 4 h with a sample rate of 340 samples/s. The resulting curve for the gyroscope of the micro-IMU is depicted in Fig. 24, and the precise characterization values for noise and drift are presented in Table IV. Comparing the three axes, the  $z$ -axis of this sensor significantly outperforms the other two axes. This effect can be explained by the MEMS nature and the geometry of the sensor. As the structures for all three axes are manufactured in one planar chip design having the  $z$ -axis orthogonal to the PCB, tradeoffs have to be made concerning the sensor quality in certain measurement axes.

Regarding the acceleration sensor shown in Fig. 25, a similar distinction between the  $z$ -axis and the other two axes can be observed. Again, the MEMS nature causes certain priority orientations; in this case, the quality of the noise in the  $x$ - and  $y$ -axis is improved. The drift of the sensor is similar in all three axes. The exact characterization values are given in Table IV.

#### E. Comparison With the Xsens MTi

We compared the micro-IMU to the Xsens MTi [14], which is a state-of-the-art commercially available IMU based on MEMS sensors and widely used in many research areas. In our comparison, we collected a set of raw data from the Xsens MTi over a period of 4 h with a data rate of 100 samples/s, which is the maximum sampling rate of the device.

We analyzed this data by means of the Allan variance. The obtained curves are shown in Figs. 26 and 27 and the precise characteristics can be found in Table IV.

As can be seen in Figs. 25 and 27, the noise values of the accelerometers are in the same range, except for the  $z$ -axis in which the MTi performs slightly better than the micro-IMU. This is due to the fact that the Xsens MTi uses a 3-D PCB design that allows placing an individual sensor for each measurement axis on one of the three orthogonally



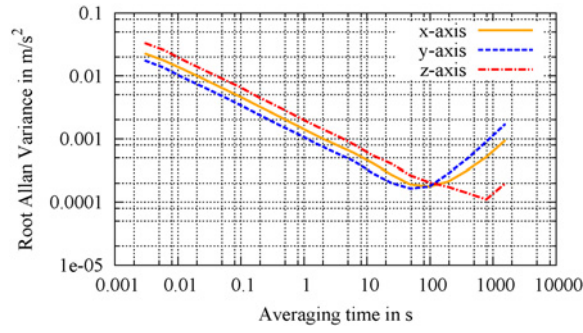


Fig. 25. Allan variance of the acceleration sensor MMA8451Q of the micro-IMU.

TABLE IV  
COMPARISON BETWEEN THE Å AND OUR MICRO-IMU

	Micro-IMU	Xsens MTi
Interface	Wireless	RS232/USB
Sampling Rate	640 sample/s	100 sample/s
Bandwidth Acc.	320 Hz	30 Hz
Bandwidth Gyro.	320 Hz	40 Hz
Power Consumption	110 mW	350 mW
Price	150 EUR (Production)	2500 EUR
Size (OEM)	22 x 14 x 4 mm <sup>3</sup>	48 x 33 x 15 mm <sup>3</sup>
Weight (OEM)	3 g	11 g
<b>Gyroscope</b>		
Noise in rad/s/ $\sqrt{\text{Hz}}$		
x-axis	0.00012	0.00070
y-axis	0.00009	0.00080
z-axis	0.00008	0.00060
Drift in rad/s		
x-axis	0.00004	0.00012
y-axis	0.00005	0.00012
z-axis	0.00002	0.00009
<b>Acceleration Sensor</b>		
Noise in m/s <sup>2</sup> / $\sqrt{\text{Hz}}$		
x-axis	0.00150	0.00090
y-axis	0.00110	0.00095
z-axis	0.00205	0.00085
Drift in m/s <sup>2</sup>		
x-axis	0.00017	0.00023
y-axis	0.00014	0.00027
z-axis	0.00011	0.00029

placed PCBs. The drift of the acceleration sensor of our micro-IMU is, on average, two times lower than that of the Xsens MTi.

For the gyroscope the micro-IMU significantly outperforms the MTi concerning drift and noise. The noise level of the micro-IMU is, on average, six times lower than that of the MTi and the drift is lower by a factor of three. Overall, despite its small size, the performance of our micro-IMU showed to be comparable to that of the Xsens MTi in an extensive static evaluation.

## V. PEDESTRIAN TRACKING APPLICATION

We demonstrate the applicability and the performance of our wireless micro-IMU in a pedestrian tracking application. In that application, we estimate the trajectory of a pedestrian whose shoe is equipped with an IMU.

Our approach to calculate the position of a pedestrian based on inertial sensors is direct integration according to [25]. The

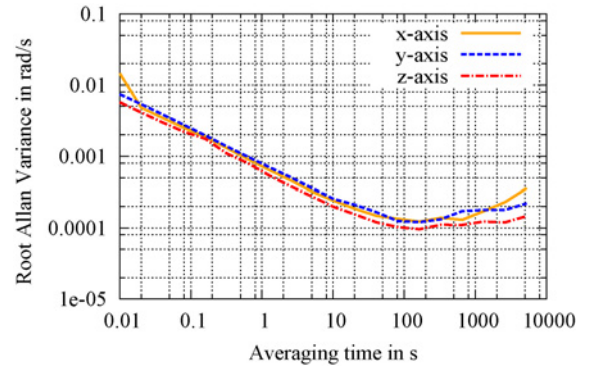


Fig. 26. Allan variance of the gyroscope of the Xsens MTi.

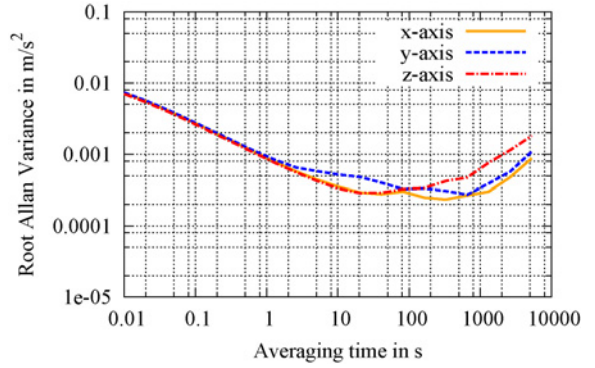


Fig. 27. Allan variance of the acceleration sensor of the Xsens MTi.

gyroscope is used to obtain the orientation data by applying the navigation equations, which were used to transfer the sensor coordinate system to the global coordinate system. After coordinate transformation of the acceleration data, the velocity and the position can be obtained by integration over time. A detailed discussion of the navigation equations can be found in [26]. However, the estimated orientation suffers from accumulating errors due to the sensor drift. Thus, a sensor data fusion with additional sensors can be used to improve the accuracy of the orientation estimates. In this study, we apply sensor data fusion based on a modified Kalman filter as described in [27]. The structure of the system is shown in Fig. 28.

In our modified Kalman filter we model the system state as the orientation error  $\delta\Theta$  and the angular rate error  $\delta\Omega$ . As measurements we use the difference between the gyro-based and the magnetic field/acceleration-based orientations. Through this state and measurement representation we avoid to model the non-linear system behavior. In the orientation estimation, the angular rate data  $\Omega$  of the three-axis gyroscope is corrected by subtracting the bias error  $\delta\Omega$  estimated from the Kalman filter based sensor data fusion, which will be mentioned in the following. Then, the gyro-based orientation  $\Theta$  is calculated from the corrected angular rate  $\hat{\Omega}$  using the navigation equations and quaternion algebra.

For the calculation of the orientation reference, we combine the three-axis magnetometer and accelerometer data to obtain another set of orientation data  $\Theta^R$ . Note that the reference orientation can be calculated only if the acceleration data is

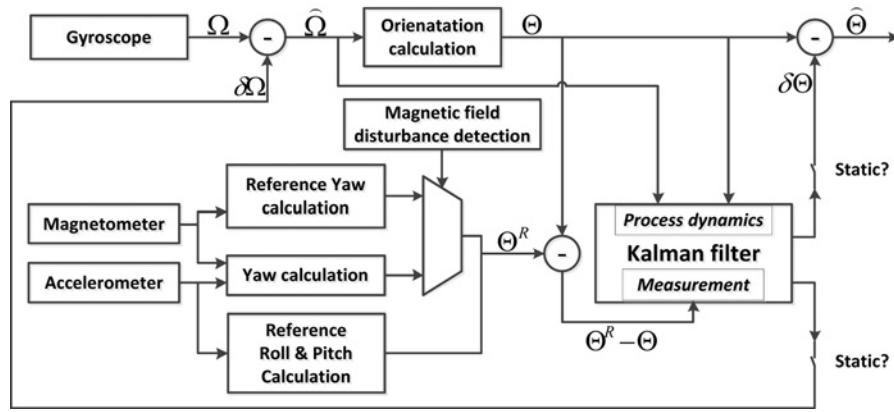


Fig. 28. Kalman filtering structure for orientation determination [27].

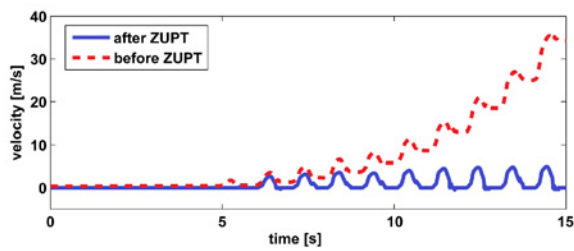


Fig. 29. Comparison between the filter estimates with and without ZUPT.



Fig. 30. For an experiment the micro-IMU was mounted on a shoe.

static, which means that the norm of the acceleration data is close to the value of the gravity. The deviation  $\Theta^R - \Theta$  between the reference orientation and the orientation estimate of the gyroscope is utilized as filter measurement to correct the state  $\delta\Theta$  and  $\delta\Omega$  estimated in the Kalman filter. After Kalman filtering, the corrected orientation  $\hat{\Theta}$  is obtained by subtracting  $\delta\Theta$  from  $\Theta$  using quaternion algebra. It can be seen that  $\hat{\Theta} = \Theta$  and  $\hat{\Omega} = \Omega$  if the acceleration data is not static. Therefore, the incorrect  $\Theta^R$  will not affect the resulted  $\hat{\Theta}$ .

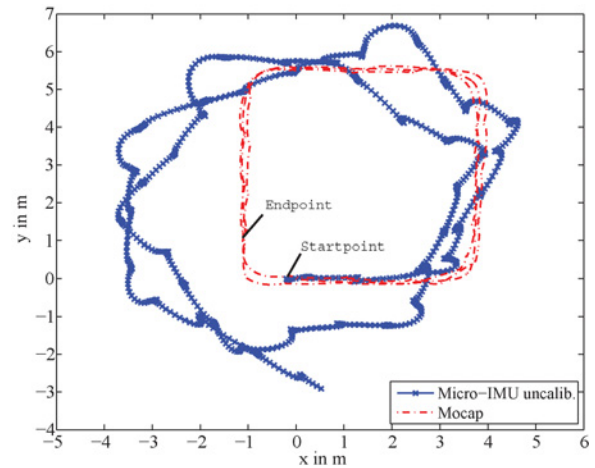


Fig. 31. Trajectory estimated from the Xsens on a walk in comparison with the true trajectory.

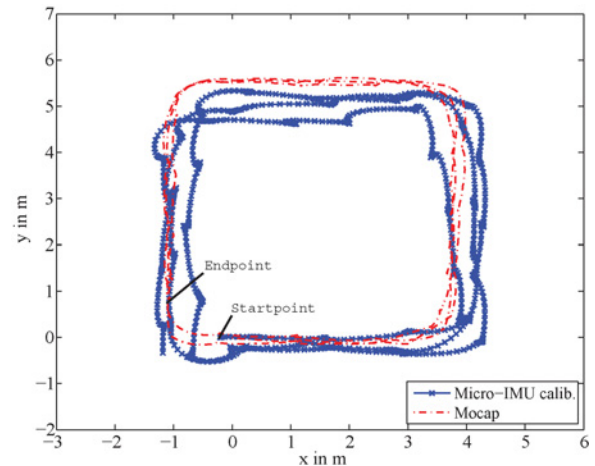


Fig. 32. Trajectory estimated from the calibrated micro-IMU on a walk in comparison with the true trajectory.

However, since the magnetic field measurements are often affected by local disturbances would result in an incorrect reference orientation  $\Theta^R$ , we detect and minimize the magnetic field disturbances in our filter. By processing the magnetic field and acceleration measurement data, magnetic disturbances can

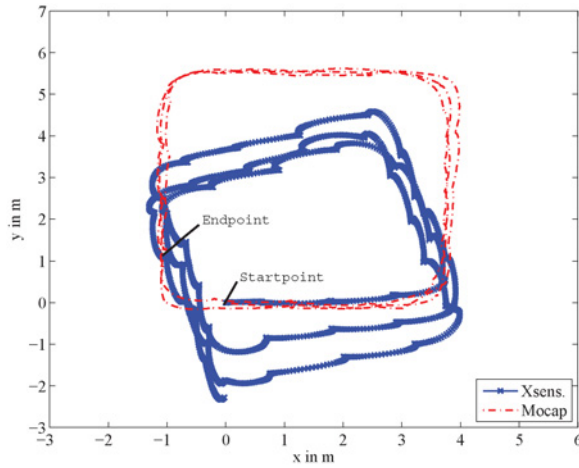


Fig. 33. Trajectory estimated from the uncalibrated micro-IMU on a walk in comparison with the true trajectory.

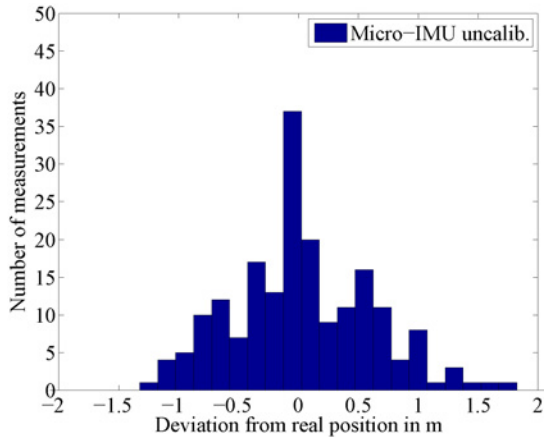


Fig. 34. Relative error deviation in 4 Hz of the uncalibrated micro-IMU (std=0.58 m).

be detected and an alternative magnetic field vector can be generated to calculate the reference orientation. In this way, the impact of disturbances can be minimized.

In our filter, the position is calculated recursively by integrating the acceleration data over time. Hence, the filter suffers from accumulating errors in the estimated translational velocity and therefore also in the estimated position. In order to deal with accumulating errors in the acceleration and the velocity, we apply the zero velocity update (ZUPT) technique [28]. In each step during normal walking, there exists the so-called still phase, a time period when the foot is not moving relative to the ground. Ojeda *et al.* [28] showed that the velocity value should be reset when the still phase is detected. We found experimentally that the best indication for the still phase can be obtained by observing the gyroscope data. If the norm of the angular rate measurement  $\Omega$  of the gyroscope is smaller than a predefined threshold, we assume that the foot is in the still phase and the velocity can be reset. In this way, the accumulation of errors in the velocity estimation can be effectively suppressed, which is shown in Fig. 29.

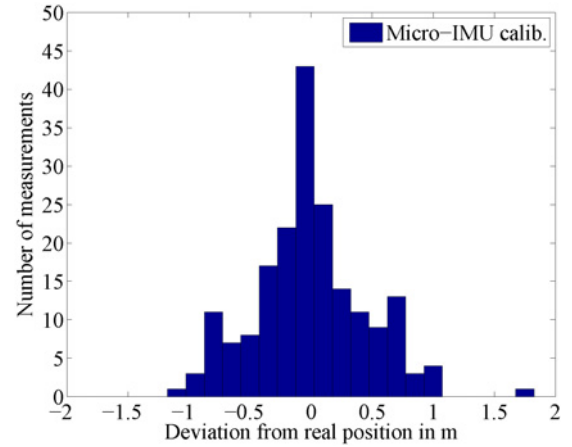


Fig. 35. Relative error deviation in 4 Hz of the calibrated micro-IMU (std=0.45 m).

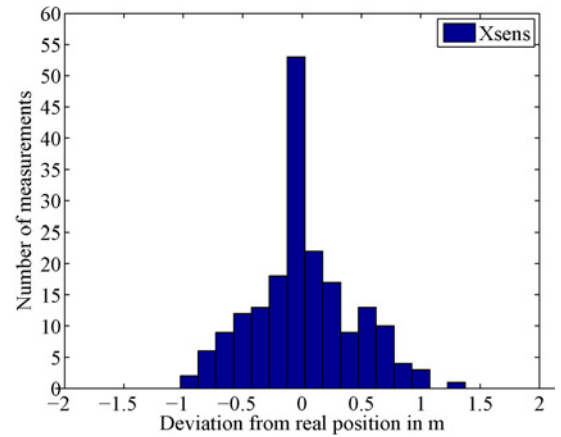


Fig. 36. Relative error deviation in 4 Hz of the Xsens MTi (std=0.48 m).

#### A. Experiment

We implemented the sensor data fusion algorithm described above and evaluated the tracking performance of our micro-IMU mounted on the toe cap of a pedestrian, as shown in Fig. 30. For comparison, we additionally mounted an Xsens MTi on the shoe. The Xsens MTi provides both Kalman filtered orientation estimates and the calibrated raw data of the individual sensors. However, in our experiments, we only used the calibrated raw data as input for the sensor data fusion algorithm. Note that this experiment focuses on the evaluation of the performance of the whole IMU in one of its common applications instead of the separate evaluation of the individual sensors employed on the IMU.

In a large experimental area in an office building, the pedestrian walked three times on a round trip, traveling a distance of about 60 m. We acquired highly accurate reference positions of the shoe using an optical motion capture system (MoCap) and compared the position and the velocity estimates of our filter algorithm to the MoCap references.

Figs. 31 and 32 show the comparison of the filter estimates using our micro-IMU and the Xsens MTi to the reference trajectory. Fig. 33 shows the trajectory estimated using the uncalibrated measurement data of the micro-IMU and Fig. 34 shows the relative deviations from the trajectory, respectively.



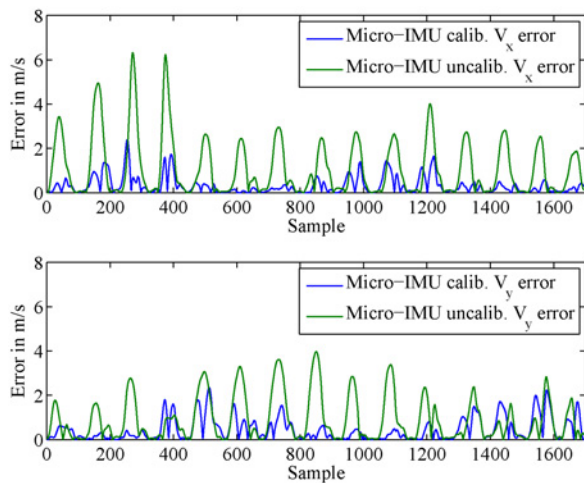


Fig. 37. Velocity error of the calibrated and uncalibrated micro-IMU.

As can be seen in Fig. 32, the calibration procedure described in Section IV-A substantially improved the quality of the measurement data and therefore enabled an accurate tracking of the pedestrian. Compared to the trajectory estimated using the measurements of the Xsens MTi, the trajectory estimated based on our micro-IMU is closer to the reference trajectory, as shown in Figs. 34–36.

We additionally evaluated the velocity error of the filter estimates with respect to the reference velocities obtained from the MoCap reference trajectory. Fig. 37 shows the x- and the y-component of the error of the velocity estimates using the uncalibrated and calibrated micro-IMU. Whereas the uncalibrated measurements of the micro-IMU result in a maximum velocity error of 6 m/s, the calibrated measurements of the micro-IMU result in a substantially lower velocity error. Overall, the results of the pedestrian tracking experiment indicate that an error compensation with calibration is inevitable for accurately tracking objects.

## VI. CONCLUSION AND FUTURE WORK

In this paper, we presented the design of a wireless micro-IMU that features minimum size and weight. By using highly integrated digital sensors and relocating data post-processing from the IMU to a base station, we were capable of competing with state-of-the-art commercial MEMS IMUs, such as the Xsens MTi. At the same time, the dimensions of the micro-IMU were considerably smaller and the static performance data of the sensors were comparable or better in terms of noise and drift. We believed that this achievement was important for an accurate tracking of people or objects in indoor environments. In the presented work, the miniature size of the designed micro-IMU made it possible to integrate the IMU into clothes or shoes. We demonstrated the calibration results and the overall performance of our micro-IMU in an extensive tracking experiment, where our micro-IMU enabled an accurate tracking of a pedestrian on a trajectory of 60 m length.

In future work, we would like to evaluate the dynamic measurement noise in a target application to improve the parameters of the filter algorithm.

## REFERENCES

- [1] B. Siciliano and O. Kathib, Eds., *Handbook of Robotics*. Berlin, Germany: Springer, 2008.
- [2] A. Bachrach, S. Prentice, R. He, and N. Roy, "RANGE: Robust autonomous navigation in GPS-denied environments," *J. Field Robot.*, vol. 28, no. 5, pp. 644–666, 2011.
- [3] A. Bry, A. Bachrach, and N. Roy, "State estimation for aggressive flight in GPS-denied environments using onboard sensing," in *Proc. IEEE Int. Conf. Robot. Autom.*, May 2012, pp. 1–8.
- [4] J. Müller, A. Rottmann, L. M. Reindl, and W. Burgard, "A probabilistic sonar sensor model for robust localization of a small-size blimp in indoor environments using a particle filter," in *Proc. IEEE Int. Conf. Robot. Autom.*, May 2009, pp. 3589–3594.
- [5] S. Grzonka, F. Dijoux, A. Karwath, and W. Burgard, "Mapping indoor environments based on human activity," in *Proc. IEEE Int. Conf. Robot. Autom.*, May 2010, pp. 476–481.
- [6] O. Bebek, M. A. Suster, S. Rajgopal, M. J. Fu, H. Xuemei, M. C. Cavusoglu, D. J. Young, M. Mehregany, A. J. van den Bogert, and C. H. Mastrangelo, "Personal navigation via high-resolution gait-corrected inertial measurement units," *IEEE Trans. Instrum. Meas.*, vol. 59, no. 11, pp. 3018–3027, Nov. 2010.
- [7] X. Yun, J. Calusdian, E. R. Bachmann, and R. B. McGhee, "Estimation of human foot motion during normal walking using inertial and magnetic sensor measurements," *IEEE Trans. Instrum. Meas.*, vol. 61, no. 7, pp. 2059–2072, Jul. 2012.
- [8] A. R. Jimenez Ruiz, F. Seco Granja, J. C. Prieto Honorato, and J. I. Guevara Rosas, "Accurate pedestrian indoor navigation by tightly coupling foot-mounted IMU and RFID measurements," *IEEE Trans. Instrum. Meas.*, vol. 61, no. 1, pp. 178–189, Jan. 2012.
- [9] H. Zhou and H. Hu, "Reducing drifts in the inertial measurements of wrist and elbow positions," *IEEE Trans. Instrum. Meas.*, vol. 59, no. 3, pp. 575–585, Mar. 2010.
- [10] L. Klingbeil, M. Romanovas, P. Schneider, M. Traechtler, and Y. Manoli, "A modular and mobile system for indoor localization," in *Proc. Int. Conf. Indoor Positioning Indoor Navigation (IPIN)*, Oct. 2010, pp. 1–10.
- [11] D. Schaefroth, S. Bouabdallah, C. Bernes, and R. Siegwart, "From the test benches to the first prototype of the muFly micro helicopter," *J. Intell. Robot. Syst.*, vol. 54, nos. 1–3, pp. 245–260, 2009.
- [12] R. J. Woods, S. Avadhanula, E. Steltz, M. Seeman, J. Entwistle, A. Bachrach, G. Barrows, S. Sanders, and R. S. Fearing, "An autonomous palm-sized gliding micro air vehicle," *IEEE Robot. Autom. Mag.*, vol. 14, no. 2, pp. 82–91, Jun. 2007.
- [13] NG LITEF. (2011). *uIMU-I* [Online]. Available: [http://www.northropgrumman.litef.com/fileadmin/downloads/Datenblatt\\_uIMU-I.pdf](http://www.northropgrumman.litef.com/fileadmin/downloads/Datenblatt_uIMU-I.pdf)
- [14] Xsens. (2011). *MTi* [Online]. Available: <http://www.xsens.com/en/general/mti>
- [15] Sparkfun. (2011). *Razor IMU* [Online]. Available: <http://www.sparkfun.com/products/10736>
- [16] x-io Technologies. (2012). *x-IMU* [Online]. Available: <http://www.x-io.co.uk/node/9>
- [17] J. Barton, A. Gonzalez, J. Buckley, B. O'Flynn, and S. C. O'Mathuna, "Design, fabrication and testing of miniaturised wireless inertial measurement units (IMU)," in *Proc. Electron. Compon. Technol. Conf.*, May 2007, pp. 1143–1148.
- [18] K. Y. Lim, F. Y. K. Goh, W. Dong, K. D. Nguyen, I.-M. Chen, S. H. Yeo, H. B. L. Duh, and C. G. Kim, "A wearable, self-calibrating, wireless sensor network for body motion processing," in *Proc. IEEE Int. Conf. Robot. Autom. (ICRA)*, May 2008, pp. 1017–1022.
- [19] Y.-L. Tsai, T.-T. Tu, and P.H. Chou, "EcoIMU: A compact, wireless, gyro-free inertial measurement unit based on two triaxial accelerometers," in *Proc. Int. Conf. IPSN*, Jun. 2011, pp. 207–212.
- [20] F. Höflinger, J. Müller, M. Törk, L. Reindl, and W. Burgard, "A wireless micro inertial measurement unit (IMU)," in *Proc. IEEE Int. Instrum. Meas. Technol. Conf. (I2MTC)*, May 2012, pp. 2578–2583.
- [21] D. H. Titterton and J. L. Weston, *Strapdown Inertial Navigation Technology*, vol. 17. Peter Peregrinus, Ltd., U.K., 2004.
- [22] J. Liu, D. Wang, H. Wang, and Y. Fan, "A rigorous approach for IMU boresight misalignment calibration," in *Proc. Int. Workshop Multi-Platform/Multi-Sensor Remote Sensing Mapping (M2RSM)*, Jan. 2011, pp. 1–4.
- [23] Honeywell International, Inc. (2012). *Magnetic Sensors* [Online]. Available: <http://www.magneticsensors.com/magnetics-faq>

- [24] N. El-Sheimy, H. Hou, and X. Niu, "Analysis and modeling of inertial sensors using Allan variance," *IEEE Trans. Instrum. Meas.*, vol. 57, no. 1, pp. 140–149, Jan. 2008.
- [25] S. Yang and Q. Li, "Inertial sensor-based methods in walking speed estimation: A systematic review," *Sensors*, vol. 12, no. 5, pp. 6102–6116, 2012.
- [26] P. Setoodeh, A. Khayatian, and E. Farjah, "Attitude estimation by separate-bias Kalman filter-based data fusion," *J. Navigation*, vol. 57, pp. 261–273, 2004.
- [27] R. Zhang and L.M. Reindl, "Pedestrian motion based inertial sensor fusion by a modified complementary separate-bias Kalman filter," in *Proc. Sensors Appl. Symp.*, Feb. 2011, pp. 209–213.
- [28] L. Ojeda and J. Borenstein, "Non-GPS navigation for security personnel and first responders," *J. Navigation*, vol. 60, no. 3, pp. 391–407, 2007.

**Fabian Höflinger** received the Master's degree in automation and energy systems from the University of Applied Sciences, Mannheim, Germany, in 2007. He is currently pursuing the Ph.D. degree in indoor-localization systems at Albert-Ludwigs University of Freiburg, Germany.

From 2007 to 2010, he was with a company for telemetric systems where he worked on inductive measurement and signal transformation. Since May 2010, he been with the Laboratory for Electrical Instrumentation, Institute of Microsystem Technology, Albert-Ludwigs University of Freiburg.

**Jörg Müller** studied computer science at the University of Freiburg, Freiburg, Germany, and received the Diploma degree in 2008.

He is currently a Research Assistant with the Albert-Ludwigs University of Freiburg, Freiburg, working in the Laboratory for Autonomous Intelligent Systems headed by Burgard. His current research interests include state estimation techniques and autonomous navigation for embedded microsystems.

**Rui Zhang** received the B.Sc. degree from the Beijing University of Aeronautics and Astronautics, Beijing, China, in July 2006, and the M.Sc. degree from the Institute of Telecommunications, Darmstadt University of Technology, Darmstadt, Germany, in May 2009.

He joined the Laboratory for Electrical Instrumentation, Institute of Microsystem Technology, Albert-Ludwigs University of Freiburg, Germany, as a Ph.D. candidate in 2009. His Ph.D. research focuses on indoor localization technologies. His current research interests include wireless infrastructure-based localization, inertial sensor-based localization, human movement monitoring, and classification.

Mr. Zhang was a recipient of the Siemens Master Program Scholarship for his Master's studies in Germany in 2006.

**Leonhard M. Reindl** (M'XX) received the Diploma degree in physics from TU Munich, Munich, Germany, in 1985, and the Dr. Sc. Techn. degree from TU Vienna, Vienna, Austria, in 1997.

In 1985, he joined the Surface Acoustic Wave (SAW) Department, Siemens Corporate Technology Division, Munich. There, he contributed to the development of SAW devices for signal processing and matched filtering in radio communications, radar systems, SAW-based identification marks, and wireless passive SAW-based sensors. In 1999, he joined the Institute of Electrical Information Technology, Clausthal University of Technology, Clausthal, Germany. In May 2003, he became a Full Professor for electrical instrumentation at the Institute for Microsystem Technology, Albert-Ludwigs University of Freiburg. He holds 45 patents on SAW devices and wireless passive sensor systems. He has authored or co-authored more than 250 papers in this field. His current research interests include wireless sensor systems, energy harvesting systems, local positioning systems, and search and rescue systems for people buried in disasters.

Dr. Reindl is a member of the Technical Programm Committees of the IEEE Frequency Control Symposium, the IEEE Ultrasonic Symposium, Eurosensors, Sensors, and the German biannual Symposium "Sensoren und Messsysteme." He was and is an Elected Member of the AdCom of the IEEE UFFC Society from 2005 to 2007 and from 2010 to 2012.

**Wolfram Burgard** studied computer science at the University of Dortmund, Dortmund, Germany, and received the Ph.D. degree in computer science from the University of Bonn, Bonn, Germany, in 1991.

He is currently a Professor of computer science with the Albert-Ludwigs University of Freiburg, Freiburg, Germany, where he heads the Laboratory for Autonomous Intelligent Systems. In the past, he and his group developed several innovative probabilistic techniques for robot navigation and control. They covered different aspects, including localization, map building, path planning, and exploration. His current research interests include artificial intelligence and mobile robots.

Dr. Burgard was a recipient of several Best Paper Awards from outstanding national and international conferences. In 2009, he was a recipient of the Gottfried Wilhelm Leibniz Prize, the most prestigious German research award. In 2010, he was a recipient of an advanced grant of the European Research Council. He is a Fellow of AAAI and ECCAI.